



Leveraging electron spin driven photocatalytic hydrogen evolution ability of BiVO₄ via crystal facet engineering and iron ion infiltration strategies

Ying Sun ^{a,1}, Jagadeesh Suriyaprakash ^{b,1}, Lianwei Shan ^{a,*}, Huanyan Xu ^{a,*}, Jiawei Zhang ^a, Guangri Chen ^a, Yinjun Zhang ^a, Haitao Wu ^{c,*}, Xuejiao Li ^a, Limin Dong ^{a,*}, Minghua Pang ^d, Dan Li ^a, Junchen Li ^a

^a Heilongjiang Provincial Key Laboratory of CO₂ Resource Utilization and Energy Catalytic Materials, School of Materials Science and Chemical Engineering, Harbin University of Science and Technology, Harbin 150040, China

^b Guangdong Provincial Key Laboratory of Nanophotonic Functional Materials and Devices, School of Information and Optoelectronic Science and Engineering, South China Normal University, Guangzhou 510006, China

^c School of Environmental and Material Engineering, Yantai University, Yantai, Shandong 264005, China

^d School of Mechanical and Electrical Engineering, Henan Institute of Science and Technology, Xinxiang 453003, China



ARTICLE INFO

Keywords:

BiVO₄
Facet
Electron spin
DFT
Photocatalysis

ABSTRACT

An electron spin regulated hydrogen evolution reaction (HER) for photocatalyst is significant to understand the underlying photocatalytic mechanism. Here, the iron with gradient distribution in BiVO₄ can successfully activate HER of Fe-BiVO₄. Mechanical performance calculations indicate that doped Fe³⁺ replacing V site can form stable chemical structure for BiVO₄. Theoretical calculations suggest that the photo-generated electrons migrate from bulk to defect sites in surface layers of Fe-BiVO₄. The doped Fe ions effectively improves the carrier transport ability and significantly reduces the carrier recombination probability. Electron spin state change of the 1Fe-BiVO₄ (Mag) enhances evidently the current density in photocatalysis, and increases markedly the HER performance compared with that of 1Fe-BiVO₄. More importantly, the magnetization further prolongs carrier lifetime and optimizes rate determining step free energy of water dissociation for Fe-BiVO₄. Our work opens a new way to understand the effect of magnetic field controlling spin states on photocatalytic HER.

1. Introduction

The worsening energy crisis and environmental issues have posed a serious threat to ecosystems over the past decades [1–3]. Nowadays, photocatalytic reactions show considerable promise in energy conversion [4,5], such as water splitting [6], CO₂ reduction [7,8], organic pollutant removal [9,10], and synthesis of H₂O₂ [11], etc. The conversion of solar energy to H₂ through photocatalytic splitting of water is one of the attractive solutions to human energy and environmental problems [12]. A large number of semiconductor materials (such as CdS [13,14] and BiVO₄ [15,16] etc) have attracted extensive attention [17]. Among them, BiVO₄ with monoclinic scheelite structure is favoured because of its suitable band gap (2.4 eV), chemical stability and harmlessness [18]. Its potential photocatalytic activity derives from Bi 6 s orbital hybridization [19]. However, the low mobility of photo-generated carriers (0.044 cm²•V⁻¹•s⁻¹) due to unconnected VO₄ remains one of

disadvantageous factors to improve the photocatalytic activity of BiVO₄ [20].

To improve the photocatalytic activity of BiVO₄, researchers have developed various strategies to solve the problems of poor charge separation and transfer efficiency, including regulation of the crystal facet [21], construction of heterojunctions [22,23], noble metal deposition [24] and ion doping [25,26]. Among them, doping can modulate the electronic structure of BiVO₄, promote charge transfer, accelerate the interfacial and bulk charge separation [27,28]. For example, Polo et al. synthesized BiVO₄ photoanodes containing Mo⁶⁺ dopant, and found that increasing the amount of Mo⁶⁺ dopant could both improve electron transport in BiVO₄ by increasing its conductivity and promote charge transfer on the electrode/electrolyte in the absence of hole scavenger [29]. Zhong et al. used In³⁺ as a dopant to replace the sites of Bi³⁺ in BiVO₄, which inhibited the surface charge recombination and enhanced the water oxidation activity on the BiVO₄ photoanode. Yin et al.

* Corresponding authors.

E-mail addresses: shlw0531@163.com (L. Shan), xuhuanyan@hrbust.edu.cn (H. Xu), wuhaitao@ytu.edu.cn (H. Wu), donglimin@hrbust.edu.cn (L. Dong).

¹ Y.S. and J.S. makes equally contributions

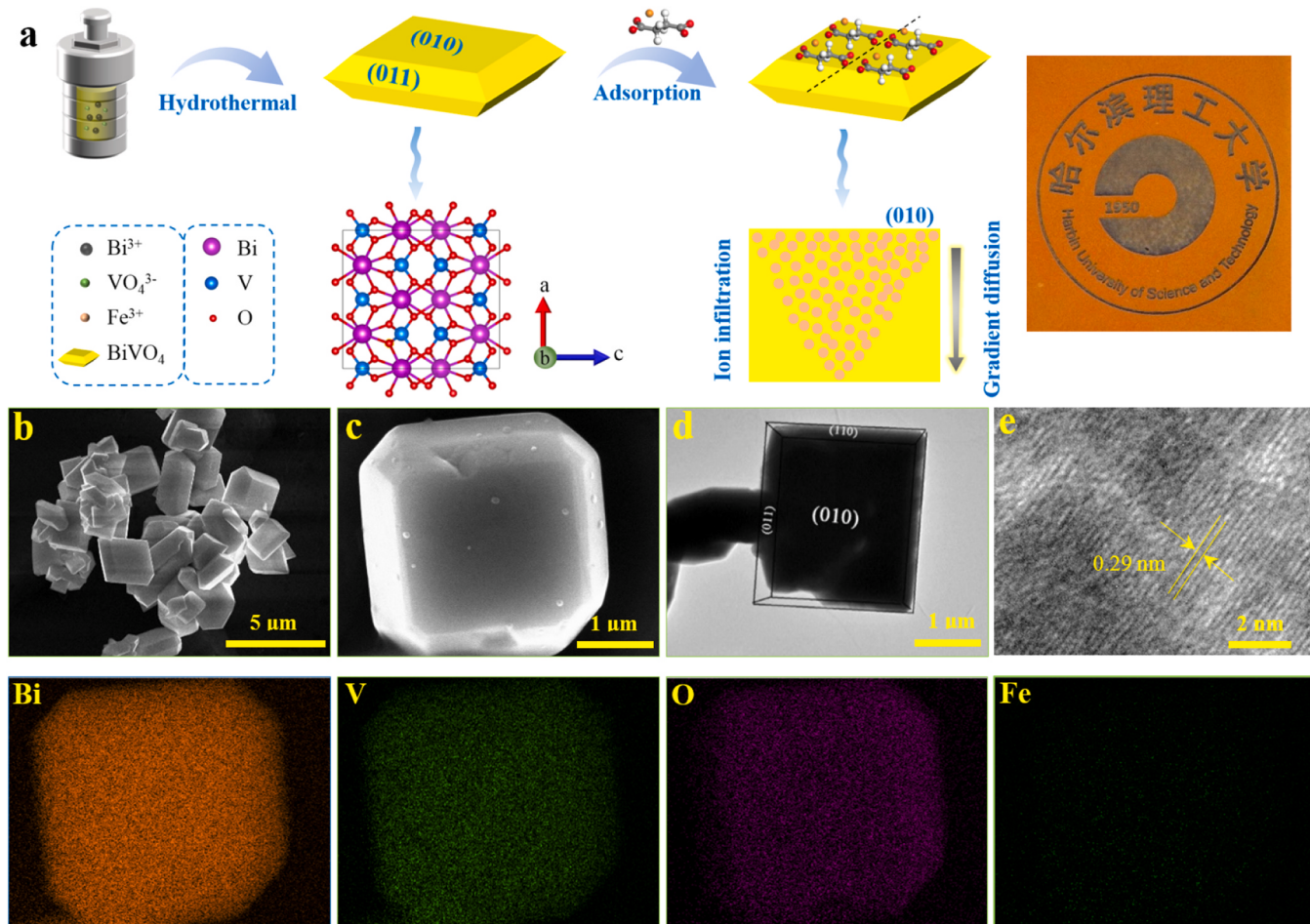


Fig. 1. (a) Schematic of the preparation process of BiVO₄ and 1Fe-BiVO₄. Right inset is optical image of 1Fe-BiVO₄. SEM images of BiVO₄ (b) and 1Fe-BiVO₄ (c). TEM (d) and HRTEM (e) images of 1Fe-BiVO₄. The element mapping images correspond to 1Fe-BiVO₄.

synthesized Mo-doped BiVO₄ films with high porosity by replacing some sites of V with Mo ions, which the photocurrent was 6.91 times higher than that of pristine BiVO₄ [30]. In addition, Regmi et al. synthesized Fe doped monoclinic BiVO₄ by microwave-hydrothermal method, which improved the visible light absorption and the photocatalytic activity [31]. The improved performance can be attributed to the efficient charge transfer and separation [32]. It looks that refining the essential scientific issues of doping and further effectively linking it with the photocatalytic hydrogen evolution performance is a fundamental scientific issue. Recently, Zhang et al. investigated the electron-hole recombination dynamics for different electron spin structures and different Ov concentrations in bulk BiVO₄ [33]. This result indicates that the spin polarization results in the suppression of its electron-hole recombination by spin protection mechanism. Several spintronics works have also shown the applied magnetic field can enhance HER and CO₂ reduction capabilities throughout the catalytic process [34–36]. Especially, further exploration is needed to understand how doping ions with spin properties can increase the electron spin state and enhance the photocatalytic hydrogen evolution performance. Therefore, it is very vital to design an effective model to embody the electron spin contribution in BiVO₄ substrate. The work on Fe³⁺ substitution of accurate metal sites in the BiVO₄ lattice is rarely mentioned. To the best of our knowledge, the regulation of electron spin state in BiVO₄ to enhance its HER activity is yet to be explored.

Considering reported work has indicated that the (010) surface of BiVO₄ has higher photocatalytic activity [37], we investigated the stability of the Fe substitution V site based on engineered (010) surface of BiVO₄. Here, the electron spin state control strategy is used to enhance

the photocatalytic hydrogen evolution performance of Fe-BiVO₄. Then, the origin of photocatalytic activity was studied through various methods such as electrochemical, optics and DFT. Finally, the effective mechanism of the electron spin state regulating photocatalytic activity in Fe-BiVO₄ is discussed in detail.

2. Experimental section

2.1. Materials and preparation

All the reagents employed were commercially available and analytically pure. They were purchased from Sinopharm Group Chemical Reagent Co. and used without any purification. 3.693 g of Bi(NO₃)₃ was dissolved in 15 mL of HNO₃ (1 M) and stirred with a magnetic stirrer until the solution became clear. The solution was named liquid A. 0.8775 g of NH₄VO₃ was dissolved in 15 mL of NaOH (2 M) and stirred with a magnetic stirrer until the solution was clear. The solution was named liquid B. Added liquid B to liquid A slowly, and adjusted the pH value of mixed solution to 7 with NaOH. Placed the mixed solution in a reaction vessel and carried out a hydrothermal reaction (180 °C for 12 h). After the washing and drying, a light yellow BiVO₄ solid powder was obtained. Magnetized BiVO₄ and 1Fe-BiVO₄ samples were named BiVO₄ (Mag) and 1Fe-BiVO₄ (Mag). Iron succinate was used as a source of iron. The dose of iron succinate was 2.67 mg mL⁻¹. First, BiVO₄ with an Fe doping mass ratio of 0.1% was prepared by placing 1.0 g of BiVO₄ into a 200 mL beaker and adding 200 mL of distilled water. Stirred in the dark for 30 min, then 0.375 mL of iron succinate was taken and added slowly to the solution. After sintering (450 °C for 3 h) above dried

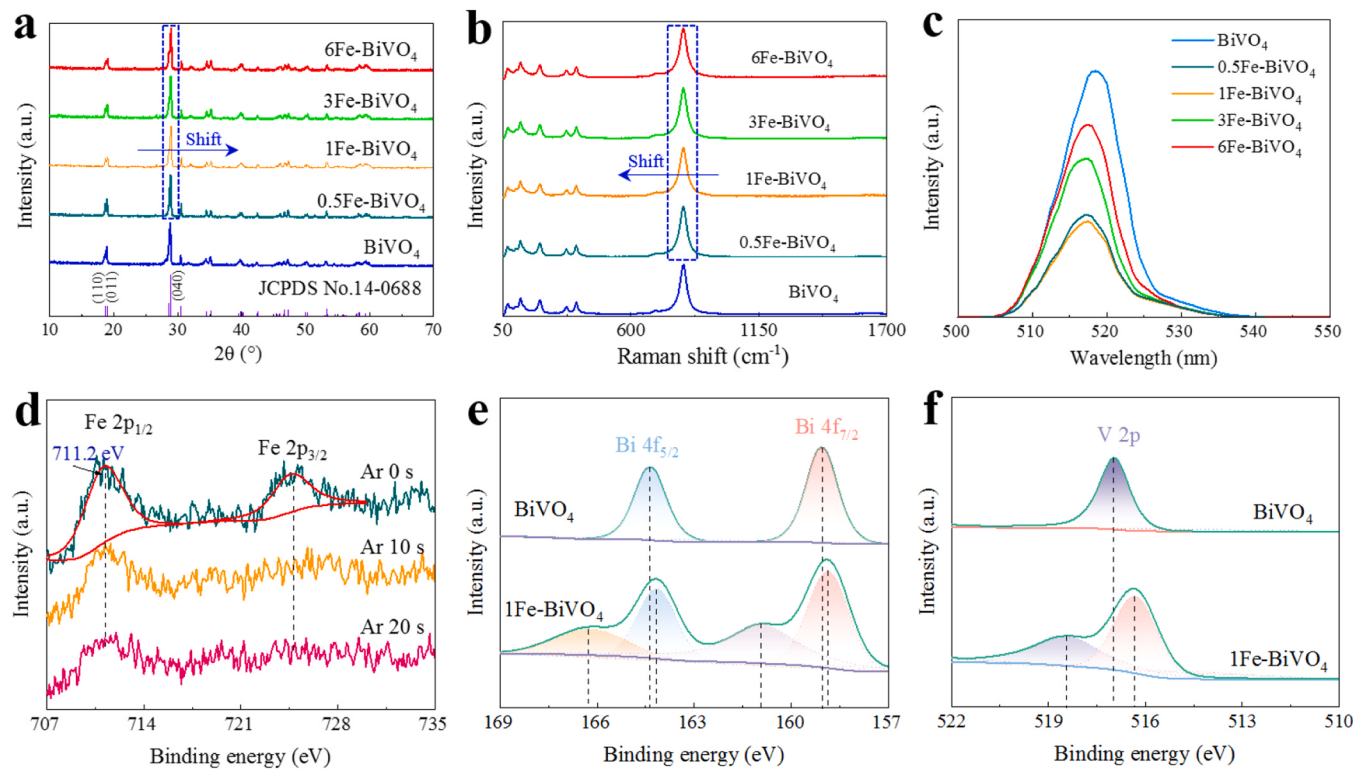


Fig. 2. (a) XRD spectra of samples. (b) Raman spectra of BiVO_4 and Fe-BiVO_4 . (c) PL spectra of BiVO_4 and Fe-BiVO_4 . (d) Evolution of Fe 2p XPS spectra as a function of Ar^+ etching time for 1Fe-BiVO_4 . High resolution XPS of Bi 4f (e) and V 2p (f) for BiVO_4 and 1Fe-BiVO_4 .

sample, obtained sample was named 1Fe-BiVO_4 . A comparable sample 1Fe BiVO_4 (h) was prepared relative to 1Fe-BiVO_4 by directly adding iron nitrate to the precursor solution. Iron-doped BiVO_4 samples with mass ratios of 0.05%, 0.3% and 0.6% were prepared according to the above method. The samples were named 0.5Fe-BiVO_4 , 3Fe-BiVO_4 and 6Fe-BiVO_4 , respectively.

2.2. Sample characterizations

The crystal structure of the samples was examined by X-ray diffractometer (XRD, X'Pert PRO), excited by $\text{Cu-K}\alpha$ radiation, and the samples were scanned in the diffraction angle range of 5–80°. The microscopic morphologies were observed by scanning electron microscopy (SEM, Apreo C) and transmission electron microscopy (TEM, JEM-2100). Photoluminescence spectra (PL) were measured by fluorescence spectrophotometer (RF-6000). Optical properties were studied by UV-Vis diffuse reflectance spectroscopy (UV-Vis DRS, UV-2600). TR-PL spectra of samples were observed by a spectrometer (FLS-1000, 325 nm excitation). The surface structures of samples were analysed by X-ray photoelectron spectroscopy (XPS, Kratos Axis Ultra DLD) with $\text{Al K}\alpha$ rays ($\hbar\nu=1486.6$ eV) as the excitation source. Raman spectroscopy was performed using an instrument (LabRAM HR) with 532 nm excitation, yielding test results of the Raman scattering peaks of the samples. The specific surface area of the samples was tested by the specific surface and pore size analyzer (3 H-2000PS2), and the Brunauer-Emmett-Teller (BET) method was used to calculate the specific surface area of the photocatalyst. The photothermal effect of samples were tested with an instrument (Fotric 225 s-V2-L24). All samples were tested for electrochemical performance using an electrochemical workstation (VMP3) with a standard three-electrode electrolysis system (reference electrode: Ag/AgCl electrode; counter electrode: Pt electrode; working electrode: conductive FTO surface coated with sample as working electrode). The equipment used for magnetizing the sample is a magnetometer (NH-20). The magnetic field is 0–5000 Oe.

2.3. Photocatalytic activity tests

Photocatalytic hydrogen production: triethanolamine was used as a sacrificial agent. 5 mL of triethanolamine and 45 mL of deionized water were mixed, and 10 mg sample to be tested was added to above solution. The prepared system was irradiated with a 300 W xenon lamp to test photocatalytic H_2 production, and after each reaction, the generated H_2 was sampled and quantified by GC-7900 gas chromatograph with a thermal conductivity detector (TCD). Argon gas was used as the carrier gas. Photocatalytic generation of H_2O_2 : 5 mg of the prepared photocatalyst was placed in 40 mL of 5% acid solution. The H_2O_2 concentration was measured with a spectrophotometer (UV-2600) and the absorbance of the intermediate solution was recorded at certain time intervals. The above steps were repeated to test the absorbance values.

2.4. Calculation details

The electronic structure (energy band structure and real space wave function) and mechanical properties (bulk elastic modulus and elastic constants) of the materials were calculated in the Vienna ab initio simulation package (VASP) using density functional theory (DFT). Dynamic properties the materials were calculated by ab initio molecular dynamics (AIMD). Simulated BiVO_4 /water and Fe-BiVO_4 /water systems with 40 explicit water molecules were utilized. We used the Nose-Hoover thermostat to balance the temperature of systems [38,39]. The cut-off energy was set to 425 eV, the convergence criterion of the force acting on each atom in the relaxation was 0.01 eV \AA^{-1} , here energy convergence criterion was 10^{-4} eV, and KPOINTS was chosen to be $3 \times 3 \times 2$. More calculation details were given in Supporting Information.

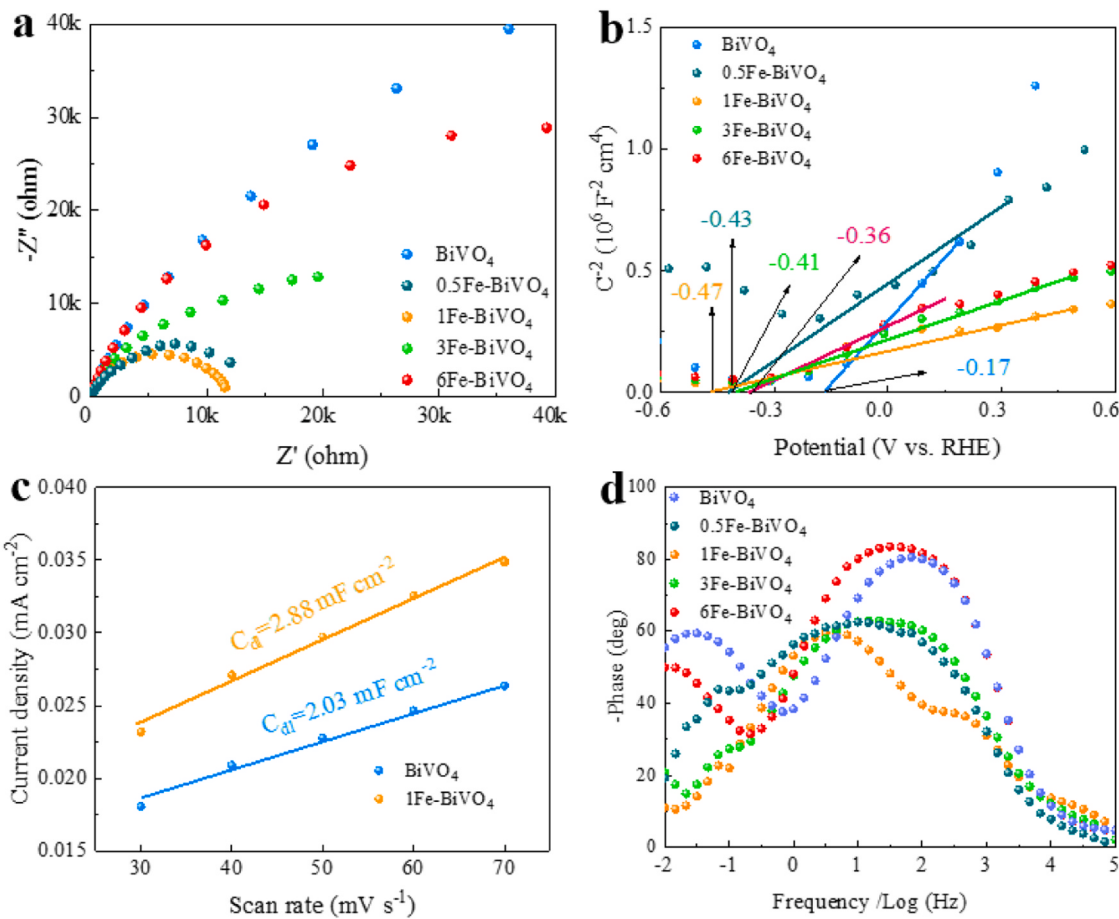


Fig. 3. (a) EIS diagram of samples. (b) Mott-Schottky diagram of samples. (c) Comparison of the bilayer capacitance of BiVO₄. (d) Bader phase angle of samples.

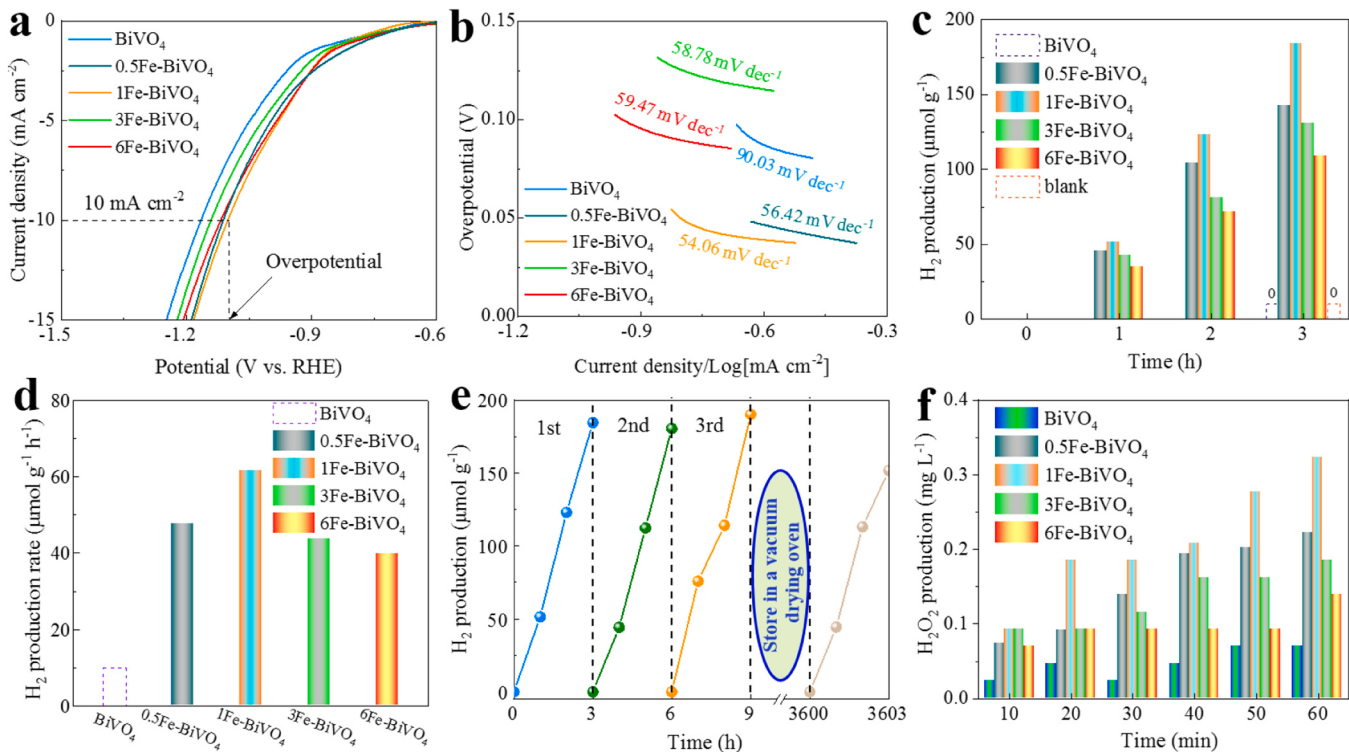


Fig. 4. Photocatalytic performance of the samples. (a) LSV curves. (b) Tafel slope. (c) Hydrogen production abilities. (d) Hydrogen production rate. (e) Cycled hydrogen production of 1Fe-BiVO₄. (f) H₂O₂ production content.

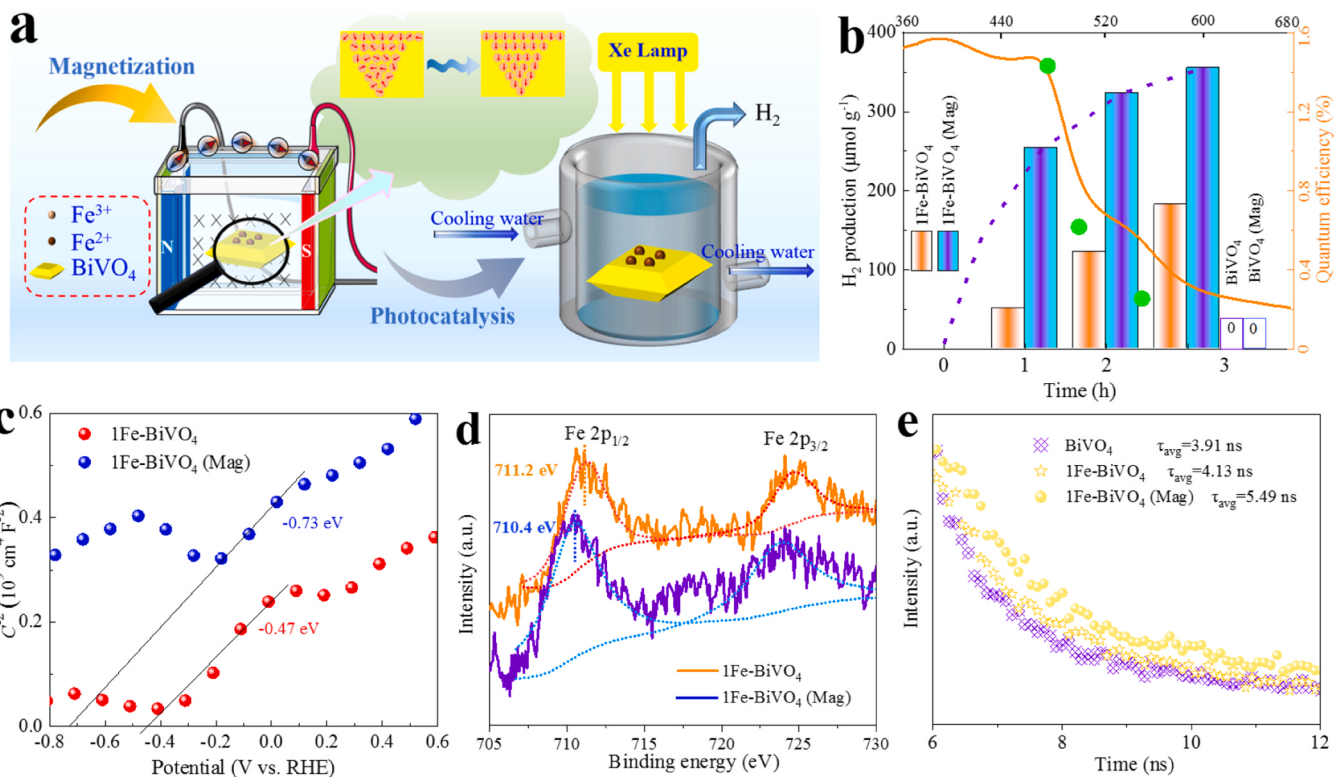


Fig. 5. (a) Magnetization treatment before photocatalytic reaction. Magnetization time is 5 min. (b) Photocatalytic hydrogen evolution. (c) Electrochemical performances for 1Fe-BiVO₄ and 1Fe-BiVO₄ (Mag).

Table 1

Comparison of the hydrogen production rate of 1Fe-BiVO₄ with other reported photocatalysts.

Photocatalysts	Sacrificial agents	Light source	H ₂ production rate (μmol g ⁻¹ h ⁻¹)	Ref.
BiVO ₄ /rGO	C ₂ H ₅ OH	200 W Hg-Xe lamp	11.50	[62]
BiVO ₄ QDs	None	300 W Xenon lamp	2.63	[63]
BiVO ₄ @TiO ₂	CH ₃ OH	300 W Xenon lamp	30.00	[64]
1Fe-BiVO ₄	TEOA	300 W Xenon lamp	61.51	This work
1Fe-BiVO ₄ (Mag)	TEOA	300 W Xenon lamp	254.36 /1 h	This work
1Fe-BiVO ₄ (Mag)	TEOA	300 W Xenon lamp	161.88 /2 h	This work
1Fe-BiVO ₄ (Mag)	TEOA	300 W Xenon lamp	118.54 /3 h	This work

3. Results and discussion

3.1. Fabrication, microstructure and electrochemical characterizations

BiVO₄ samples were prepared by hydrothermal method as shown in Fig. 1a. In a typical synthesis, Fe-BiVO₄ samples were prepared by infiltration strategy. SEM and TEM images show that BiVO₄ and 1Fe-BiVO₄ samples are decahedral structures with highly exposed (010) facets (Figs. 1b-d). As can be seen, the BiVO₄ before and after doping is plate feature. Note that the main exposed surface of the crystal surface is the (010) facet. The doping of Fe does not affect the morphology of BiVO₄. HRTEM image confirmed that the lattice distance of 0.29 nm (Fig. 1e), indicating that the main crystal facet of 1Fe-BiVO₄ is (010) facet [40,41]. The subsequent element mapping images confirm the uniform distribution of each element in the system. However, direct

addition of Fe³⁺ during hydrothermal process disrupts the regular morphology growth of 1Fe-BiVO₄ (h) crystal (see Fig. S1).

The crystal structures of BiVO₄ and Fe-BiVO₄ show that there are four major diffraction peaks at 18.67°, 18.99°, 28.82° and 30.55° (Fig. 2a), corresponding to the (110), (011), (-121) and (040) crystal plane diffraction peaks of BiVO₄, respectively. The diffraction peaks of both BiVO₄ and Fe-BiVO₄ conform to the monoclinic structure of BiVO₄ (ICSD No. 14-0688), but some diffraction peaks of Fe-BiVO₄ are slightly shifted to higher diffraction angle. This may be due to fact that the radius of Fe³⁺ ion (1.17 Å) is smaller than that of V⁵⁺ ion (1.22 Å), and the Fe element can be doped into the lattice of BiVO₄. The Fe-doping produces a slight lattice contraction. Detailed XRD peak shifting of sample can be seen in Fig. S2. And there are no other diffraction peaks in the XRD pattern of Fe-BiVO₄. In addition, direct addition of Fe³⁺ during hydrothermal process can maintain the monoclinic structure of 1Fe-BiVO₄ (h) crystal (Fig. S3). As shown in Fig. 2b, Raman spectroscopy analysis of the prepared samples observed vibrational peaks at about 208.2 cm⁻¹, 367.4 cm⁻¹ and 824.3 cm⁻¹ for both BiVO₄ and Fe-BiVO₄ samples, which is consistent with previous reports [42]. For BiVO₄ photocatalyst, the characteristic band at 824.3 cm⁻¹ is assigned to asymmetric and symmetric forms of V-O bond stretching vibrations [43]. Furthermore, a reduction of vibration frequency was observed for the Fe-BiVO₄ samples. Fig. S4 gives the detailed Raman peak shifting of samples. It suggests that the Fe-O bond has strong covalent bonding interactions, leading to a change in the degree of electron localization. PL is caused by the recombination of photo-generated electron-hole pairs, which can reflect the features of carrier separation, transfer and migration [44]. Fig. 2c shows the PL spectra of the samples under 260 nm light excitation. The BiVO₄ sample has an intense emission peak at 516 nm, while the PL intensities of the Fe-BiVO₄ samples are significantly lower than that of the pure BiVO₄ sample, which signifies a higher separation efficiency of photo-generated carriers in Fe-BiVO₄ samples. The chromaticity coordinates of BiVO₄ and Fe-BiVO₄ samples show slightly different color gamut, indicating that the PL colors of the

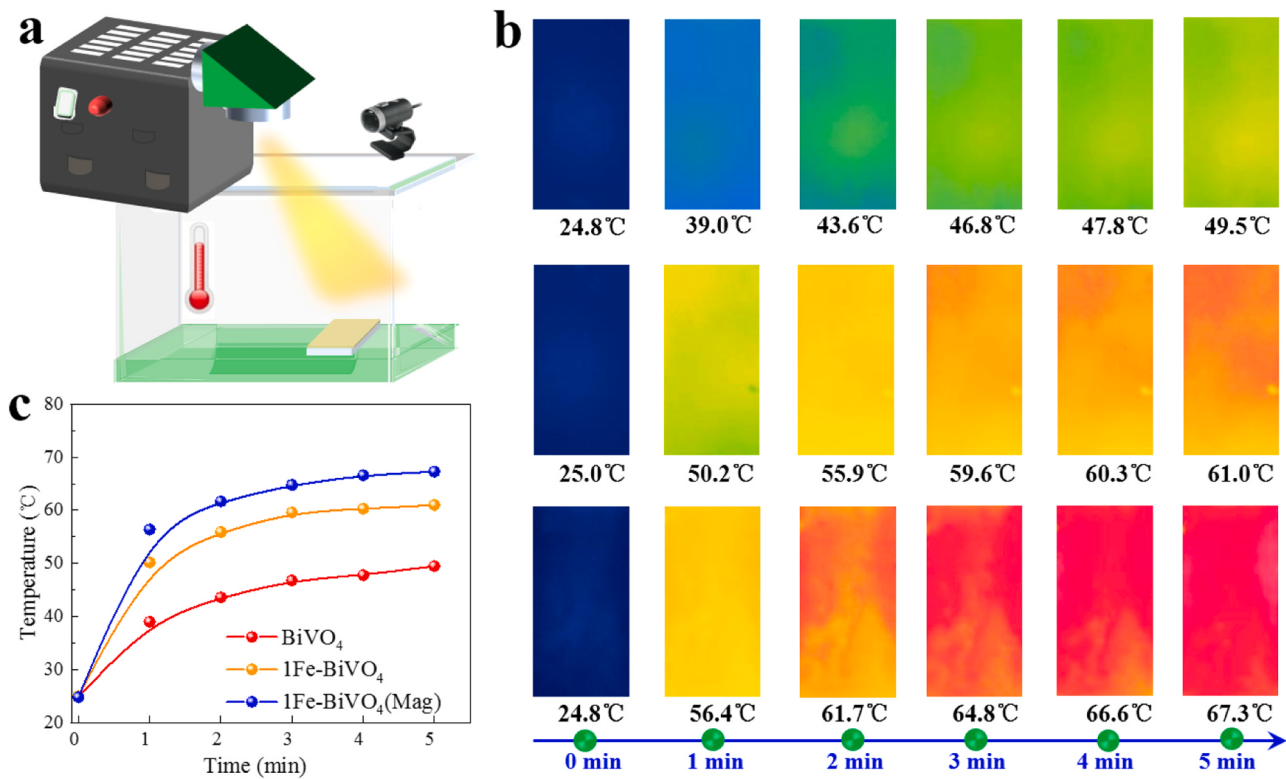


Fig. 6. (a) Schematic diagram of photothermal effect. (b) Surface temperature variation of samples under 300 W xenon lamp irradiation. (c) Temperature variation trend of samples.

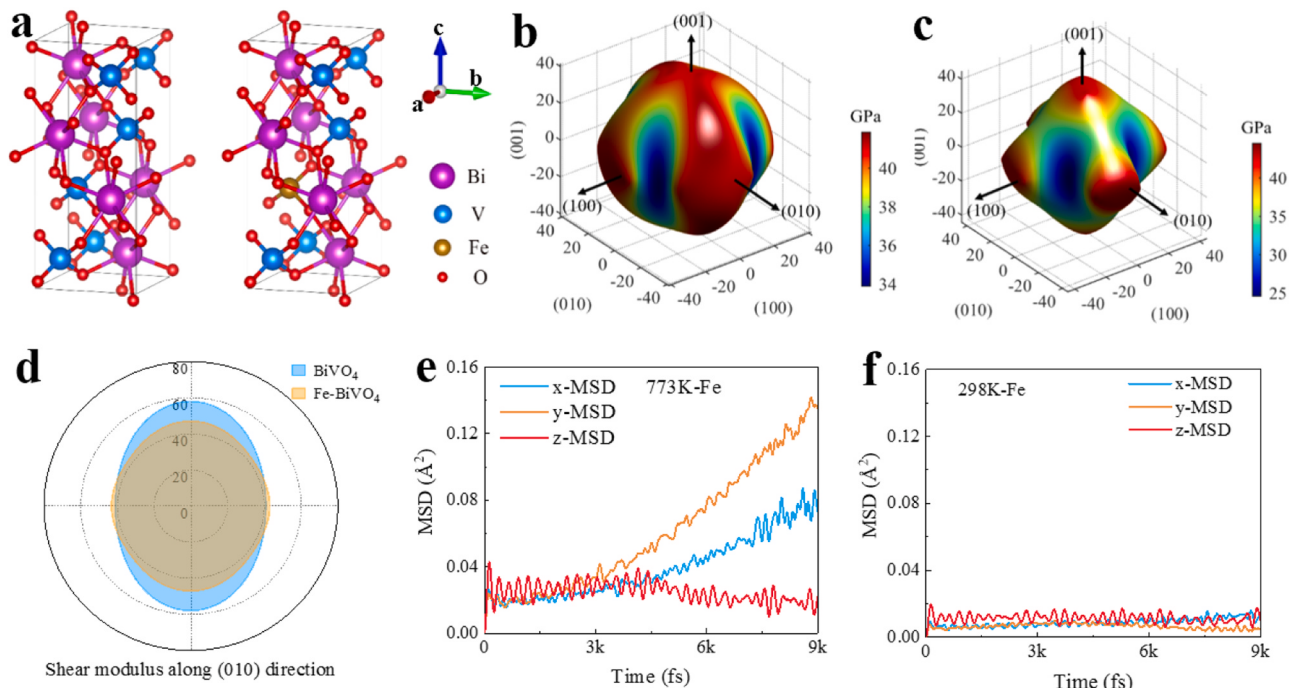


Fig. 7. (a) Cell models of BiVO₄ and Fe-BiVO₄. (b) 3D surfaces of shear modulus of (a) BiVO₄ and (b) Fe-BiVO₄. (c) 2D projection of shear modulus of BiVO₄, Fe-BiVO₄ along the (010) direction. (d) Shear modulus along (010) direction. (e) MSD of Fe³⁺ with simulation time (773 K). (f) MSD of Fe element (298 K).

samples before and after doping change to some extent (Fig. S5).

To confirm Fe distribution in the surface of the BiVO₄, the 1Fe-BiVO₄ sample was subjected to XPS depth profiling technique by Ar⁺ etching (Fig. 2d). As can be seen from the figure, the curve corresponding to 0 s clearly shows that the binding energies of the 2p orbitals of iron ion are

711.2 eV and 725.01 eV, respectively, indicating that the ion is mainly present in the form of Fe³⁺ in Fe-BiVO₄ [41,45]. When the Ar⁺ etching time increased to 10 s and 20 s, the intensity of the characteristic peak of Fe³⁺ became significantly lower. Therefore, the content alteration of Fe in the sample presents a gradient distribution. The surface chemical

Table 2C_{ij} values of BiVO₄ and Fe-BiVO₄.

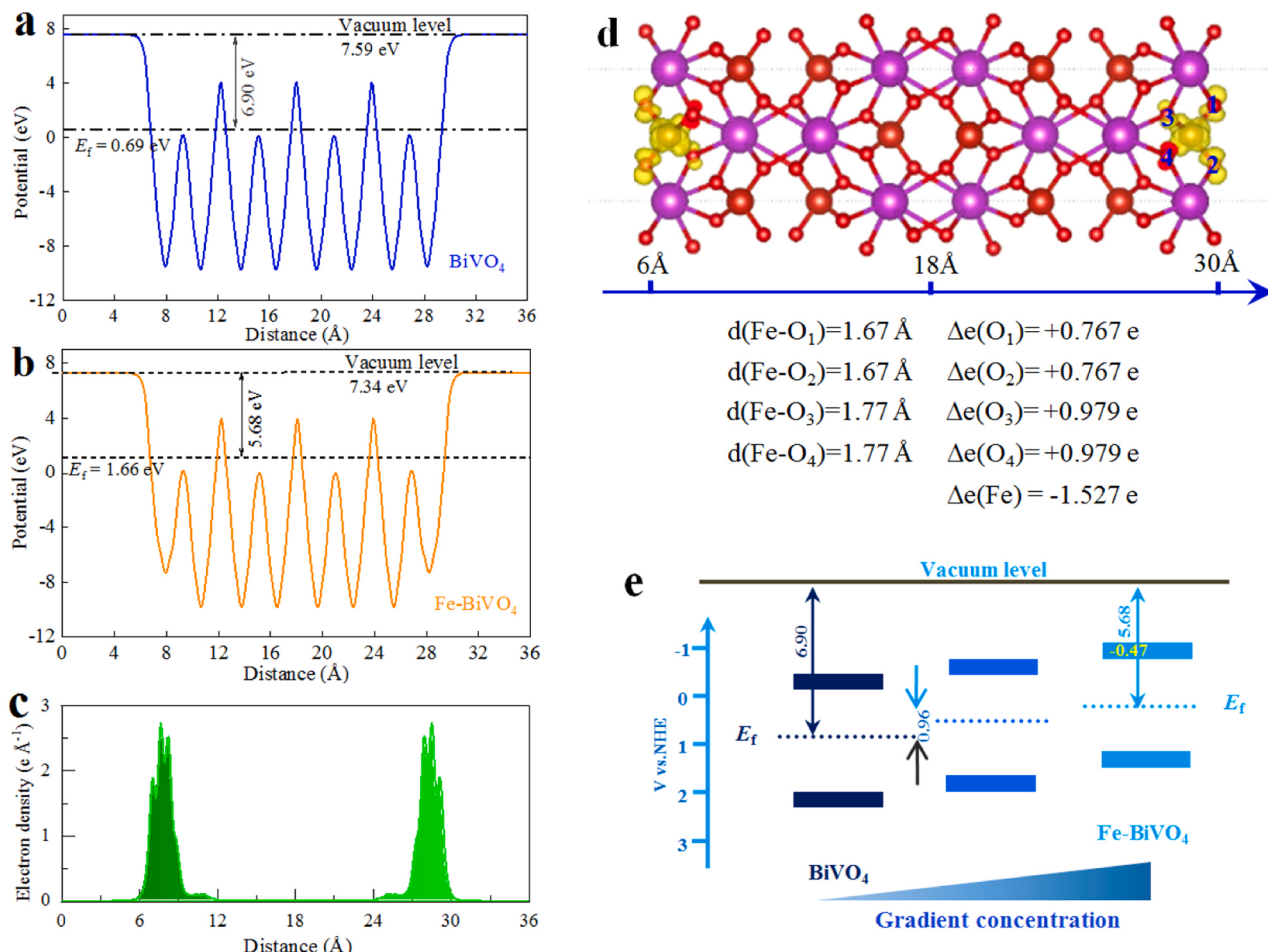
Substitution site		C _{i1}	C _{i2}	C _{i3}	C _{i4}	C _{i5}	C _{i6}
Fe→Bi	C _{1j}	149.89	43.64	5.78	-5.39	-43.28	16.93
	C _{2j}	43.64	149.35	-8.77	-3.98	-29.35	-32.59
	C _{3j}	5.78	-8.77	39.26	-4.81	-33.97	-10.74
	C _{4j}	-5.39	-3.98	-4.81	18.46	-16.74	2.22
	C _{5j}	-43.28	-29.35	-33.97	-16.74	-89.13	20.71
	C _{6j}	16.93	-32.59	-10.74	2.22	20.71	45.58
Fe→V	C _{1j}	190.09	116.13	98.24	0.00	0.00	20.36
	C _{2j}	116.13	181.26	94.52	0.00	0.00	-19.78
	C _{3j}	98.24	94.52	166.06	0.00	0.00	-0.14
	C _{4j}	0.00	0.00	0.00	44.51	-0.05	0.00
	C _{5j}	0.00	0.00	0.00	-0.05	41.79	0.00
	C _{6j}	20.36	-19.78	-0.14	0.00	0.00	64.36

Table 3Calculated B_H, G_H, the ratio of G_H/B_H, E, and m of BiVO₄ with/without oxygen vacancy.

Materials	B _H (GPa)	G _H (GPa)	E (GPa)	m	B _H /G _H
BiVO ₄	129.74	45.63	122.53	0.34	2.84
Fe-BiVO ₄	127.59	42.70	115.25	0.35	2.99

composition and chemical states of the BiVO₄ and 1Fe-BiVO₄ samples were determined by XPS (Figs. 2e, f). The presence of Bi, V, O and Fe elements on the sample surface was detected (Fig. S6). In the Bi 4 f XPS spectra (Fig. 2e), the BiVO₄ sample has two strong peaks at 164.4 eV and

159.1 eV belonging to Bi 4 f_{5/2} and Bi 4 f_{7/2} [46], corresponding to Bi³⁺. Compared to the BiVO₄ sample, the 1Fe-BiVO₄ sample has a shift of 0.2 eV in the position of Bi 4 f_{5/2} (164.2 eV) and Bi 4 f_{7/2} (158.9 eV). The peaks at 160.9 and 166.3 eV with higher binding energy can be attributed to Bi^{3+x} ions [47], which is because the doped Fe cannot provide enough valence electrons. In Fig. 2f, the V 2p binding energy in BiVO₄ is 516.9 eV [48], demonstrating the presence of element V in the form of V⁵⁺ [49]. Compared to the BiVO₄ sample, we can observe a shift of 0.3 eV (V 2p orbital binding energy of 516.6 eV) in the 1Fe-BiVO₄ sample, in addition to the presence of an additional peak at the binding energy of 518.5 eV, indicating that the iron doping in V site leads to a local elevation and decrease in the chemical state of its adjacent V

**Fig. 8.** (a, b) Calculated electrostatic potentials of BiVO₄ and Fe-BiVO₄. (c) Photo-generated electron density of Fe-BiVO₄. (e) Surface energy band gradient variation of Fe-BiVO₄.

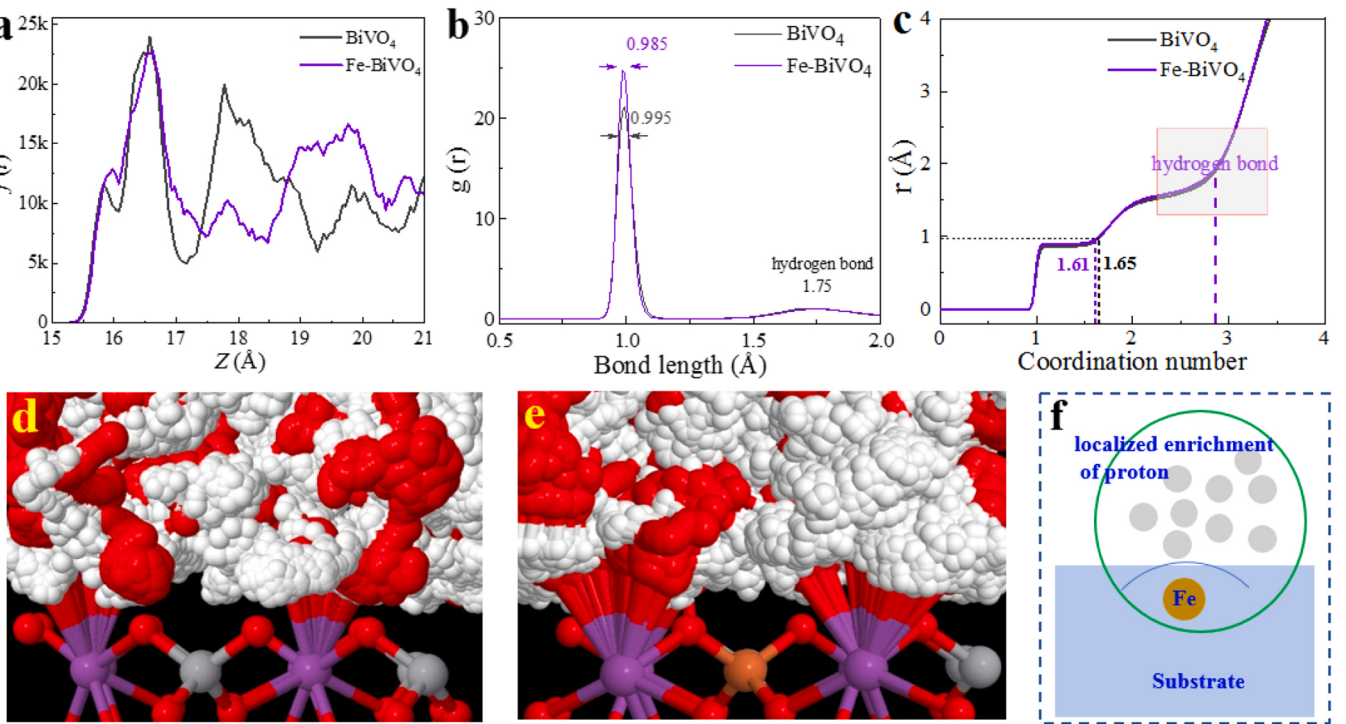


Fig. 9. Statistical results of H₂O molecules in BiVO₄/H₂O and Fe-BiVO₄/H₂O. (a) Hydrogen distribution along c axis. (b) Radial distributions in BiVO₄ and Fe-BiVO₄. (c) Coordination number of H₂O in systems. AIMD trajectory evolutions of BiVO₄/H₂O (d) and Fe-BiVO₄/H₂O (e). (f) Localized enrichment of proton in near the doping site.

element. Such change is more favorable for the formation of stable structure. It can provide local polarization, which promote carrier transport and separation.

The different samples show a various response in the visible region (Fig. S7). One can find that the visible range of BiVO₄ is the smallest, while the visible absorption range of Fe-BiVO₄ increases, which may be due to the enhanced absorption of light by lattice distortion. A large slope in the visible region suggests that the absorption of visible light is caused by the band gap transition of the material itself. The reported work has shown that BiVO₄ is a direct band-gap semiconductor [50]. The band gap is 2.48 eV and 2.42 eV for BiVO₄ and 1Fe-BiVO₄, respectively. Fig. S8 shows the N₂ adsorption-desorption isotherms and pore size distribution curves of BiVO₄ and 1Fe-BiVO₄. The isotherm shapes of both samples are similar with the type IV isotherm curves [51, 52]. When the relative nitrogen pressure was increased from 0 to one atmosphere, the nitrogen adsorption amounts of BiVO₄ and 1Fe-BiVO₄ were also increased to 25.9 cm³/g and 28.6 cm³/g, respectively. Table S1 shows the BET specific surface area of BiVO₄ and 1Fe-BiVO₄, where the specific surface area of 1Fe-BiVO₄ is 6.56 m²/g. The slightly higher specific surface area can promote the adsorption of reactants to some extent [53].

The charge mobility inside the semiconductor is one of the important factors affecting the photocatalytic activity. The radius of the electrochemical impedance (EIS) curve reflects the charge transfer resistance [54]. Fe-BiVO₄ has the smaller radius than that of BiVO₄ (Fig. 3a), implying a lower resistance. 1Fe-BiVO₄ has the smallest radius, suggesting that the low charge transfer resistance in 1Fe-BiVO₄ is favourable to the transport of photo-generated carriers. Fig. 3b shows Mott-Schottky (M-S) curves of samples. The slopes of the M-S curves of both BiVO₄ and Fe-BiVO₄ are positive, indicating that they are n-type semiconductors [55]. The flat-band potentials of BiVO₄, 1Fe-BiVO₄, 3Fe-BiVO₄ and 6Fe-BiVO₄ are -0.17 eV, -0.47 eV, -0.41 eV and -0.36 eV, respectively, and the flat-band potentials of n-type semiconductors can be approximated as the conduction band (CB) potential [56]. The CB potential of the sample is more negative than the redox

potential of the standard hydrogen electrode, which satisfies the thermodynamic prerequisite in the photocatalytic hydrogen production from water. Notably, the gradient Fe doping makes the CB of Fe-BiVO₄ shift to a more negative position compared with 1Fe-BiVO₄ (h) sample (Fig. S9). A shift of the CB position to a more negative direction can enhance the drive force of reduction reaction ability from thermodynamic aspect [57].

The electrochemical active surface area (ECSA) of the materials was studied by testing the non-Faraday window of the cyclic voltammetry (CV) curve, and the double-layer capacitance (C_{dl}) of the catalyst was shown in Fig. 3c (also see Fig. S10). The C_{dl} of 1Fe-BiVO₄ is larger than that of BiVO₄, indicating that 1Fe-BiVO₄ has a higher active surface area with more active sites [58], which improves the photocatalytic hydrogen production performance. Here, we also used characteristic maximum frequency (*f*_{max}) to reflect the relation between structure and carrier lifetime (Fig. 3d). Due to the inverse relationship between carrier lifetime and characteristic frequency (*τ*, time constant, *τ*=1/2π*f*_{max}) [59], it is inferred that the lifetime of free electrons in the 1Fe-BiVO₄ sample is longer than that of other samples.

3.2. Photocatalytic performances and photothermal effect

As shown in Fig. 4a, BiVO₄ shows a high overpotential when reaching a current density of 10 mA cm⁻², so the pure BiVO₄ sample has poor catalytic activity for hydrogen evolution rate (HER). Fe-BiVO₄ shows a relatively small overpotential at 10 mA cm⁻², indicating that iron doping can effectively reduce the HER overpotential, sharply accelerate the kinetics of the H⁺ reduction reaction and significantly improve the hydrogen evolution activity. To further investigate the reaction kinetics of HER of BiVO₄ with Fe-BiVO₄, the Tafel curves of BiVO₄ and Fe-BiVO₄ were tested (Fig. 4b). The Tafel slopes of BiVO₄, 1Fe-BiVO₄, 3Fe-BiVO₄ and 6Fe-BiVO₄ were 90.03 mV dec⁻¹, 54.06 mV dec⁻¹, 58.78 mV dec⁻¹ and 59.47 mV dec⁻¹, respectively. The smaller Tafel slope, the faster current density increases, which means the reaction kinetic process is faster [60]. Compared with BiVO₄, Fe-BiVO₄ has a

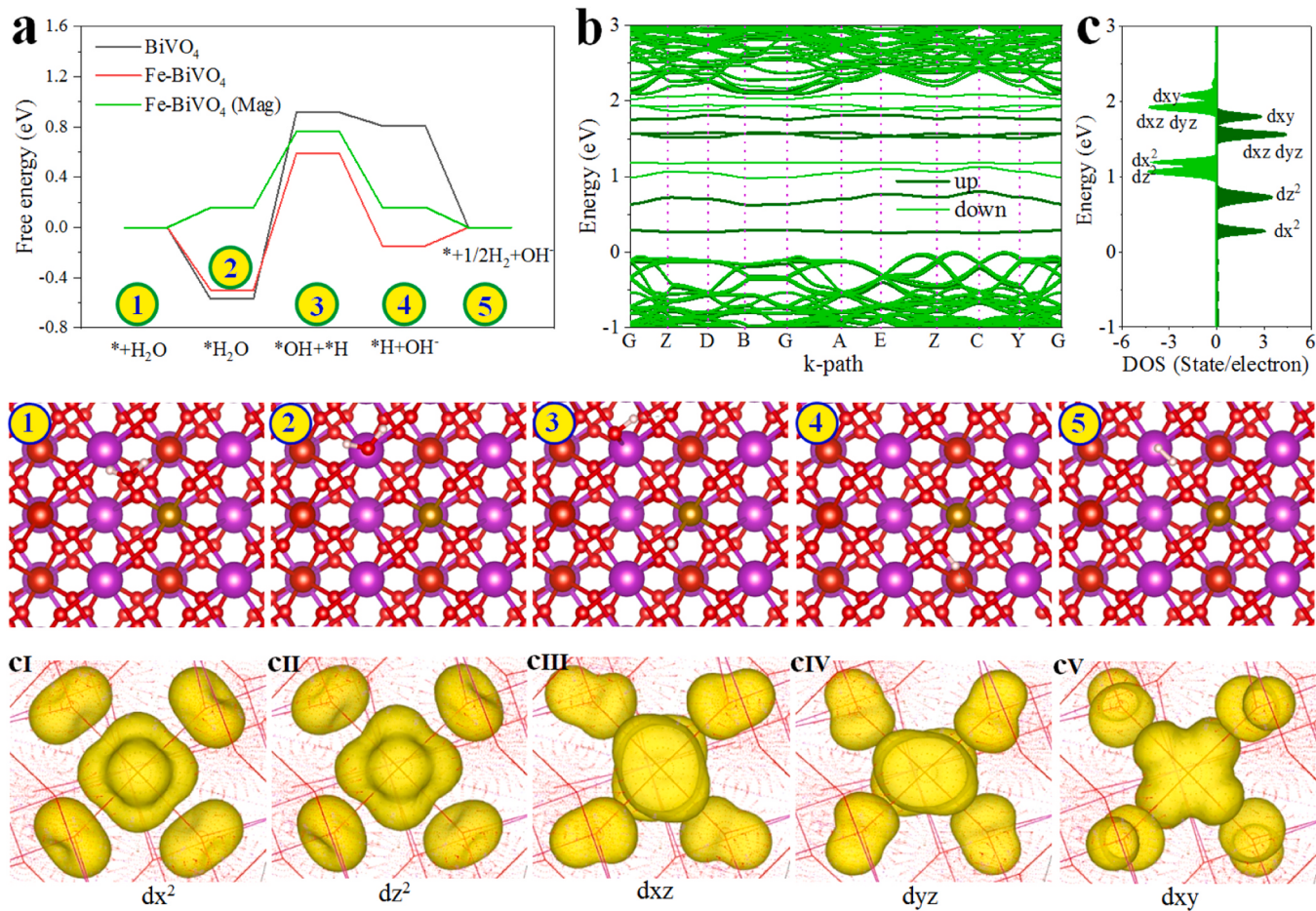


Fig. 10. (a) Calculated the free energy of water dissociation for BiVO₄, Fe-BiVO₄ and Fe-BiVO₄ (Mag). Arabic numeral (1–5) here correspond to different adsorption configurations. For instance, the second configuration corresponds to the *H₂O adsorption state. (b) Energy band structure of Fe-BiVO₄. Fermi level is set as zero. (c) Spin orbital coupling of Fe 3d. (cI–cV) Fe 3d orbitals in Fe-BiVO₄.

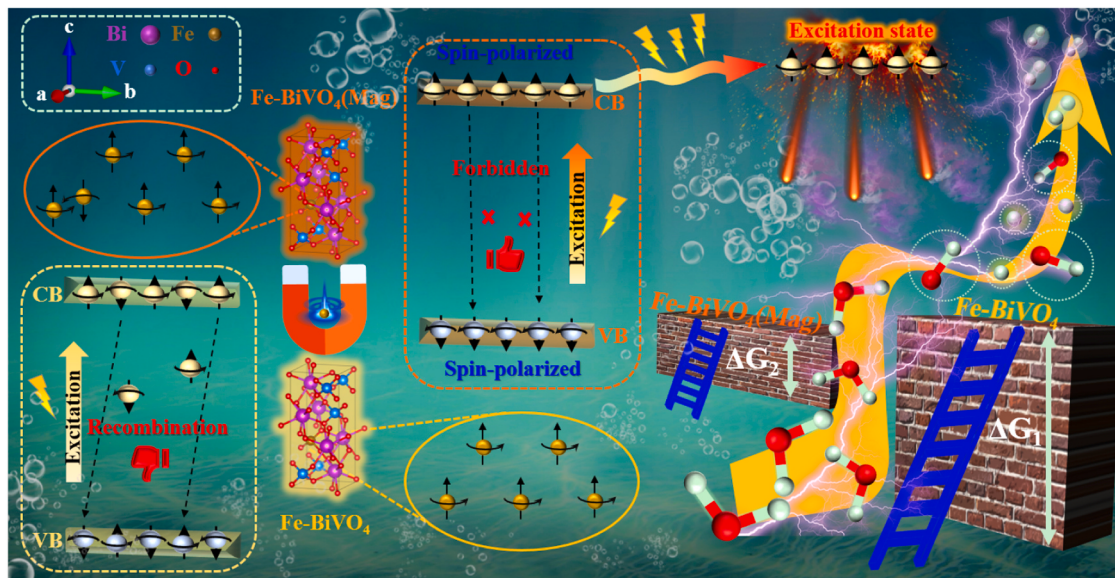


Fig. 11. Proposed photocatalytic mechanism driven by electron spin state.

lower Tafel slope, indicating that Fe-BiVO₄ has higher carrier density, which is associated with excellent reaction kinetics. The photocatalytic hydrogen production capacity of the prepared samples was evaluated. It

can be seen from Fig. 4c that Fe-BiVO₄ has higher hydrogen production than BiVO₄ within 3 h. Here, a blank test was performed in the absence of photocatalyst. It was found that the hydrogen production in the

solution of triethanolamine and water without catalyst was zero, indicating that triethanolamine as an electron sacrificial agent can effectively prevent the recombination of electron-hole pairs, thus providing an indication for the structural modulation of BiVO_4 . The HER rate of Fe-BiVO_4 was significantly higher than that of BiVO_4 (Fig. 4d). The hydrogen production rate of 1Fe-BiVO_4 is $61.51 \mu\text{mol g}^{-1} \text{h}^{-1}$. The results indicate that Fe^{3+} doping can effectively open and improve the photocatalytic splitting of water for BiVO_4 ($0 \mu\text{mol g}^{-1} \text{h}^{-1}$), evidencing that Fe^{3+} is a proper dopant for BiVO_4 .

In Fig. 4e, the hydrogen evolution rates of the 1Fe-BiVO_4 maintain a stable state for three consecutive cycles, indicating that the photocatalytic activity of 1Fe-BiVO_4 has stable hydrogen evolution performance. The hydrogen evolution performance of the sample was tested again after 3600 h (in a vacuum drying oven). It was observed that the hydrogen evolution performance of the sample slightly decreased, but still had good hydrogen evolution activity, which showed that 1Fe-BiVO_4 had excellent chemical stability and good cycled stability of hydrogen evolution (also see Fig. S11, S12). And the HER ability of 1Fe-BiVO_4 is significantly higher than that of 1Fe-BiVO_4 (h) sample (Fig. S13). The photocatalytic H_2O_2 production abilities of the samples were examined under simulated visible light irradiation with formic acid solution as sacrificial agent (Fig. 4f). The rate of H_2O_2 production for the BiVO_4 sample was $0.07 \text{ mg L}^{-1} \text{ h}^{-1}$. The relatively higher H_2O_2 production abilities were provided over Fe-BiVO_4 , among which the rate of for 1Fe-BiVO_4 reached $0.32 \text{ mg L}^{-1} \text{ h}^{-1}$. The schematic diagram of magnetization is shown in Fig. 5a. The applied magnetic field changes the spin state of doped iron elements in BiVO_4 . The device used is shown in Fig. S14. Here, the magnetization was performed for BiVO_4 and 1Fe-BiVO_4 samples, and photocatalytic hydrogen evolution experiments were conducted (Fig. 5b). The results indicate that the photocatalytic hydrogen evolution performance of BiVO_4 remains almost unchanged before and after magnetization. For magnetized 1Fe-BiVO_4 (Mag) sample, the photocatalytic hydrogen evolution performance is significantly improved compared to the unmagnetized 1Fe-BiVO_4 . At the first hour, it shows a 4-fold HER ability compared to 1Fe-BiVO_4 . At this time, the quantum efficiency is close to 1.5%, which is as high as reported $\text{Pt}^{\text{II}}/\text{C}_3\text{N}_4$ system [61]. At the third hour, HER ability of 1Fe-BiVO_4 (Mag) is still 2 times higher than that of 1Fe-BiVO_4 . Overall, it is a functional relationship, y (hydrogen evolution) = $(-362.38 \pm 9.97) \times e^{-t/(0.84 \pm 0.07)} + (362.69 \pm 8.07)$. The electrochemical results indicate that the reduction ability of photo-generated electrons is significantly improved after magnetization for 1Fe-BiVO_4 . The magnetization control of the 1Fe-BiVO_4 before the photocatalytic hydrogen evolution reaction changed the spin state of iron in the sample. Essentially, enable electron deficient iron ions to receive more carrier replenishment. Electrochemically, it exhibits a left shift in the flat band potential (Fig. 5c). To confirm the magnetization role, we investigated the chemical state doped Fe in the 1Fe-BiVO_4 sample (Fig. 5d). As can be seen, the curve of 1Fe-BiVO_4 shows that the binding energy of 711.2 eV ($2\text{p } 1/2$) corresponds the Fe^{3+} . When the magnetization is applied, the binding energy of the this peak shifts to 710.4 eV , which agrees with $\text{Fe}^{(3-\delta)+}$. The significantly lower binding energy indicates that the magnetization effectively regulates the electron spin state in 1Fe-BiVO_4 (Mag) sample (also see Fig. 11).

We used TR-PL to explore the effect of magnetization on carrier lifetime of 1Fe-BiVO_4 (Fig. 5e). The average lifetime τ_{avg} of Fe-BiVO_4 and 1Fe-BiVO_4 is 3.91 ns and 4.13 ns , respectively. Nevertheless, the τ_{avg} is prolonged to 5.49 ns for 1Fe-BiVO_4 (Mag). It evidences that the proper spin state can impede the recombination of carrier. Then the longer carrier lifetime in 1Fe-BiVO_4 (Mag) provides the larger probability of electron participating in the HER. Table 1 shows the comparison of the photocatalytic hydrogen evolution rates of 1Fe-BiVO_4 with those of previously reported photocatalysts. Different researchers used different sacrificial agents to study the hydrogen evolution performance of photocatalysts, for example, when ethanol was used as a sacrificial agent, and the photocatalytic HER rate of BiVO_4/rGO is $11.5 \mu\text{mol g}^{-1}$

h^{-1} [62].

To explore the relation between electron spin and the photothermal effect, we used several samples with obvious comparability to evidence photothermal conversion features (Fig. 6a). Under the irradiation of 5 min, the BiVO_4 , 1Fe-BiVO_4 and 1Fe-BiVO_4 (Mag) show different temperature variation (Figs. 6b, c). For 1Fe-BiVO_4 (Mag), the surface temperature reaches to 67.3°C , which is higher than BiVO_4 (49.5°C) and 1Fe-BiVO_4 (61.0°C). This suggests that the doped iron has prompted the strong photothermal effect. Thus, it indicates that the thermoelectric current ($I = dQ/dt$) of 1Fe-BiVO_4 is higher than that of BiVO_4 . More importantly, the magnetization further increases the thermoelectric current of the 1Fe-BiVO_4 . Significantly, the magnetization can regulate the carrier density or transport properties for 1Fe-BiVO_4 . More photothermal results on FTO and samples are provided in Fig. S15.

3.3. Structural stability, surface potential and solid/liquid interface characteristics

The cell models of BiVO_4 and Fe-BiVO_4 are shown in Fig. 7a. In these structures, each vanadium atom is attached to four oxygen atoms, called V-O bonds, and each bismuth atom is attached to eight oxygen atoms, called Bi-O bonds [65]. As we known, there are two metal sites (Bi and V) in BiVO_4 . In order to evidence replacing probability of Fe^{3+} , we considered two cases of Fe^{3+} doping in Bi or V site. The elastic constants C_{ij} of both cases were obtained by DFT calculation in Table 2. For monoclinic lattice, the Born elastic stability criteria [66] are recorded in the supporting information. The calculations show that the Fe^{3+} substitution for V satisfies the stability criterion for the mechanical properties of the BiVO_4 , while the Fe^{3+} substituting Bi site can cause instability of BiVO_4 . As the iron replacing Bi site in bismuth vanadate (Table S2), the $\lambda_1 = -110.84 < 0$. This indicates that the eigenvalue of the stiffness matrix does not meet elastic constant stability criteria. However, for BiVO_4 or Fe-BiVO_4 (Fe-V), the eigenvalue of the stiffness matrix can meet elastic constant stability criteria. More information on structural stability of BiVO_4 and Fe-BiVO_4 , please see Fig. S16-S18.

Considering the arithmetic average relation of the effective modulus [67], the values of bulk modulus B_H , shear modulus G_H , the ratio of B_H/G_H , Young's modulus E, and Poisson's ratio were obtained according to the Voigt-Reuss-Hill (VRH) approximation, and the calculated results are listed in Table 3. As $B_H/G_H > 1.75$ [68], the material will exhibit ductility. The values of B_H/G_H for both BiVO_4 and Fe-BiVO_4 are greater than 1.75, indicating that BiVO_4 and Fe-BiVO_4 are structurally stable.

The results derived from the ELAM code [69] depict the 3D surface of the shear modulus and the 2D projection on the (010) direction (Figs. 7b-d). The 3D surface shows that both BiVO_4 and Fe-BiVO_4 have severely aspheric surfaces (Figs. 7b, c), indicating that they both have high shear modulus anisotropy. The greater deviation of the projected pattern of the elastic modulus, the higher degree of anisotropy of the solid material in that plane [70]. Along the (010) direction, BiVO_4 exhibits a large deviation (Fig. 7d), indicating a high shear modulus anisotropy. Thus the (010) facet of Fe-BiVO_4 exhibits a local asymmetric structure property. Figs. 7e and f give the ion migration characteristics in BiVO_4 samples by calculating the mean square displacement (MSD). It shows the variation of the Fe element diffusion with simulation time, where the y-direction corresponds to the diffusion direction of Fe element along the (010) direction. It is noticed that the diffusion rate of Fe element is the largest in the (010) direction (773 K). It indicates that Fe element is more likely to enter the lattice of BiVO_4 from (010) facet. This indicates that the designed BiVO_4 with (010) facet is an excellent substrate for Fe element diffusion. AIMD simulation performed at 298 K suggests that Fe element has the lowest diffusion rate in (010) direction, indicating that (010) facet is more stable at room temperature.

Figs. 8a and b show the variations of the electrostatic potential energy of the BiVO_4 and Fe-BiVO_4 along the vertical surface direction. The potential energy curve in the vacuum region is a flat, which indicates that the potential energy function has converged in the vacuum region.

The Fermi level of Fe-BiVO₄ (1.66 eV) is higher than that of BiVO₄ (0.69 eV). This difference in work function derives from charge accumulation in the iron enriched area in BiVO₄. Due to the Fe-doped BiVO₄ has a higher Fermi energy level, it indicates that Fe-BiVO₄ has more electrons in equilibrium compared with BiVO₄. The photo-generated electron density of Fe-BiVO₄ was calculated using DFT (Figs. 8c, d). The yellow represents the electron accumulation region, which evidences the increased electron cloud density. This suggests that the directional transfer of electrons from the bulk phase of BiVO₄ to the surface area enriched with iron. Bader charge calculation indicates that locally doped iron loses 1.527 e (Fig. 8d). By further calculating the Bader charges of iron oxide (monoclinic phase and hexagonal phase), we find that the iron ions lose 1.323 e and 1.349 e, respectively (Figs. S19, S20). These results indicate that the doped iron ion in BiVO₄ is trivalent. Based on the theoretical calculations mentioned above, the gradient potential and Fermi level distribution characteristics on the surface of Fe-BiVO₄ induced by iron doping are presented here (Fig. 8e). Overall, iron doping effectively promotes the effective transfer of photo-generated electrons from bulk to surface defect sites.

Fig. 9a shows the distribution of hydrogen elements on the surfaces of BiVO₄ and Fe-BiVO₄. Compared to the surface of BiVO₄, iron doping in the surface can significantly enrich hydrogen to propel the possibility of HER. In the BiVO₄/H₂O and Fe-BiVO₄/H₂O systems, there is also a slight difference in the hydrogen oxygen bond length for water molecules (Fig. 9b), and the bond length in the Fe-BiVO₄/H₂O system is substantially lower than that in the BiVO₄/H₂O system. If the hydrogen oxygen bond length is the same, the coordination number of H₂O in Fe-BiVO₄/H₂O system is markedly smaller than that of oxygen in BiVO₄/H₂O system (Fig. 9c), indicating that water is more easily dissociated in Fe-BiVO₄/H₂O system. We investigated the AIMD trajectories of BiVO₄/H₂O and Fe-BiVO₄/H₂O (Figs. 9d, e). It is observed that there are differentiated distribution characteristics of hydrogen elements. Iron doping site promotes localized enrichment of hydrogen (Fig. 9f), which is caused by the attraction of protons generated by the local electron enrichment effect.

3.4. Electron spin driven photocatalytic mechanism

Fig. 10a shows the hydrogen evolution free energy of different systems. It can be seen that the BiVO₄ and Fe-BiVO₄ systems exhibit spontaneous adsorption of water. For all systems, the dissociation process of water is a non-spontaneous process. This also indicates that the dissociation reaction of water is a rate determining step for all systems. The dissociation free energy of water is 1.48, 1.09 and 0.61 eV in BiVO₄, Fe-BiVO₄ and Fe-BiVO₄ (Mag), respectively. Fig. 10b shows the energy band structures of BiVO₄ and Fe-BiVO₄. BiVO₄ exhibits the semiconductor properties of the indirect band gap (Fig. S21). The multiple energy levels generated by doped iron fill the bandgap space of BiVO₄ (Fig. 10b). Iron doping forms local splitting of the spin orbitals at the bottom of the BiVO₄ CB, and affects the CB of BiVO₄. For example, at point G, a clear splitting originates from the 6p orbital splitting of Bi atoms in BiVO₄. This interaction among spin orbitals is beneficial for the spatial transition of photo-generated electrons between doping sites and adjacent metal sites. The d-orbital in the doping site undergoes a typical spin orbital splitting, and the order of energy levels is $d_{xy} > d_{xz} = d_{yz} > d_{z^2} > d_{x^2}$ (Fig. 10c). Their real spatial orbitals are shown in the Fig. 11c1-c5. Here, the spin splitting of d orbital adjacent to the CB can evidently drive the carrier transport within the Fe-BiVO₄ system.

Fig. 11 gives the photocatalytic mechanism driven by electron spin state. For BiVO₄, the iron doping can decrease overpotential, prolong carrier lifetime, and activate HER. Simultaneously, it can also reduce the dissociation reaction free energy of water to some extent. Significantly, magnetization enhances substantially the reduction ability of photo-generated electrons, prolongs markedly carrier lifetime, and boost evidently thermoelectric current. It is worth noting that magnetization changes the water adsorption free energy of Fe-BiVO₄, and it approaches

0. More importantly, the magnetization can prominently optimize the dissociation free energy of water. It indicates that the adjustment of local electron spin states can significantly increase the carrier lifetime efficiently regulate the photocatalytic hydrogen evolution performance of Fe-BiVO₄.

4. Conclusion

In summary, we achieved an electron spin regulated hydrogen evolution reaction for Fe-BiVO₄. DFT calculations indicate that doped Fe³⁺ replacing V site can form stable chemical structure for BiVO₄. It indicates that the doped Fe³⁺ can activate HER of Fe-BiVO₄ compared to negligible hydrogen production of BiVO₄. Theoretical calculations evidence that the defect sites in surface layers of Fe-BiVO₄ can enrich the photo-generated electrons. The results proclaim that the Fe ions doping effectively improves the carrier transport ability and significantly reduces the carrier recombination probability. The 1Fe-BiVO₄ (Mag) increases tremendously the photocatalytic hydrogen evolution performance compared with that of 1Fe-BiVO₄. And, the relationship between photocatalytic hydrogen evolution and reaction time conforms to the y (hydrogen evolution) = $(-362.38 \pm 9.97) \times e^{-t/(0.84 \pm 0.07)} + (362.69 \pm 8.07)$ function. It is confirmed that the magnetization can enhance the current density in photocatalysis for the 1Fe-BiVO₄. Additionally, we find that the magnetization further prolongs the carrier lifetime and optimizes the rate determining step free energy of water dissociation (0.61 eV) for Fe-BiVO₄. This work highlights a new viewpoint to understand the effect of electron spin on photocatalytic hydrogen evolution performance.

CRediT authorship contribution statement

Ying Sun: Writing – original draft, Investigation, Data curation. **Jagadeesh Suriyaprakash:** Writing – review & editing, Methodology, Investigation. **Lianwei Shan:** Writing – review & editing, Supervision, Project administration, Investigation, Formal analysis, Conceptualization. **Huanyan Xu:** Methodology, Conceptualization. **Jiawei Zhang:** Investigation, Data curation. **Guangri Chen:** Investigation, Data curation. **Yinjun Zhang:** Visualization, Data curation. **Haitao Wu:** Methodology, Conceptualization. **Xuehao Li:** Methodology, Investigation. **Limin Dong:** Methodology, Conceptualization. **Junchen Li:** Investigation, Data curation. **Minghua Pang:** Methodology, Investigation. **Dan Li:** Methodology, Investigation.

Declaration of Competing Interest

There are no conflicts to declare.

Data availability

Data will be made available on request.

Acknowledgements

The authors gratefully acknowledge financial supports from the Nature Scientific Foundation of Heilongjiang Province (LH2023E081), Ecological and Environmental Protection Research Project of Heilongjiang Province (HST2022S010, HST2023QT003) and Natural Science Foundation of Shandong Province (ZR2021LSW014). Jagadeesh Suriyaprakash (JS) acknowledges China Postdoctoral Science Foundation (2020M672669). We thank the Resources provided by Ph. D. Yangtao Zhou (Chinese Academy of Sciences).

Declaration of Competing Interest

There are no conflicts to declare.

Appendix A. Supporting information

Supplementary data associated with this article can be found in the online version at doi:10.1016/j.apcatb.2024.124209.

References

- [1] R. Poudyal, P. Loskot, R. Nepal, R. Parajuli, S.K. Khadka, Mitigating the current energy crisis in Nepal with renewable energy sources, *Renew. Sust. Energ. Rev.* 116 (2019) 109388.
- [2] B. Li, H.-Y. Xu, Y.-L. Liu, Y. Liu, Y. Xu, S.-Q. Zhang, Unveiling the structure–activity relationships of ofloxacin degradation by Co_3O_4 -activated peroxyomonosulfate: from microstructures to exposed facets, *Chem. Eng. J.* 467 (2023) 143396.
- [3] S.K. Batabyal, S.E. Lu, J.J. Vittal, Synthesis, characterization, and photocatalytic properties of In_2S_3 , ZnIn_2S_4 , and CdIn_2S_4 nanocrystals, *Cryst. Growth Des.* 16 (2016) 2231–2238.
- [4] L. Gan, G. He, Y. Liu, W. Li, J. Li, Engineering heteropolyblue hole transfer layer for efficient photoelectrochemical water splitting of BiVO_4 photoanodes, *Appl. Catal. B: Environ. Energy* 349 (2024) 123895.
- [5] Y. Zhang, J. Zhao, H. Wang, B. Xiao, W. Zhang, X. Zhao, T. Lv, M. Thangamuthu, J. Zhang, Y. Guo, J. Ma, L. Lin, J. Tang, R. Huang, Q. Liu, Single-atom Cu anchored catalysts for photocatalytic renewable H_2 production with a quantum efficiency of 56, *Nat. Commun.* 13 (2022) 58.
- [6] M.Z. Xie, X.D. Fu, L.Q. Jing, P. Luan, Y.J. Feng, H.G. Fu, Long-lived, visible-light-excited charge carriers of $\text{TiO}_2/\text{BiVO}_4$ nanocomposites and their unexpected photoactivity for water splitting, *Adv. Energy Mater.* 4 (2014) 1300995.
- [7] J. Bian, J. Feng, Z. Zhang, Z. Li, Y. Zhang, Y. Liu, S. Ali, Y. Qu, L. Bai, J. Xie, D. Tang, X. Li, F. Bai, J. Tang, L. Jing, Dimension-matched zinc phthalocyanine/ BiVO_4 ultrathin nanocomposites for CO_2 reduction as efficient wide-visible-light-driven photocatalysts via a cascade charge transfer, *Angew. Chem. Int. Ed.* 58 (2019) 10873–10878.
- [8] J. Yang, X. Zhao, S. Bu, W. Fan, Theoretical insights into the role of metal–support interactions of an Al_2O_3 -supported Ru_4 cluster in CO_2 dissociation, *J. Phys. Chem. C* 122 (2018) 17287–17300.
- [9] H.-Y. Xu, S.-Q. Zhang, Y.-F. Wang, Y. Xu, L.-M. Dong, S. Komarneni, New insights into the photocatalytic mechanism of pristine ZnO nanocrystals: from experiments to DFT calculations, *Appl. Surf. Sci.* 614 (2023) 156225.
- [10] S. Singla, S. Sharma, S. Basu, MoS_2/WO_3 heterojunction with the intensified photocatalytic performance for decomposition of organic pollutants under the broad array of solar light, *J. Clean. Prod.* 324 (2021) 129290.
- [11] Y. Isaka, Y. Kawase, Y. Kuwahara, K. Mori, H. Yamashita, Two-phase system utilizing hydrophobic metal–organic frameworks (MOFs) for photocatalytic synthesis of hydrogen peroxide, *Angew. Chem. Int. Ed.* 58 (2019) 5402–5406.
- [12] L. Shan, Z. Fang, G. Ding, Z. Shi, L. Dong, D. Li, H. Wu, X. Li, J. Suriyaprakash, Y. Zhou, Y. Xiao, Electron confinement promoted the electric double layer effect of $\text{BiOI}/\beta\text{-Bi}_2\text{O}_3$ in photocatalytic water splitting, *J. Colloid Interf. Sci.* 653 (2024) 94–107.
- [13] L. Cheng, Q. Xiang, Y. Liao, H. Zhang, CdS -based photocatalysts, *Energy Environ. Sci.* 11 (2018) 1362–1391.
- [14] L. Shan, M. Yuan, J. Zhang, G. Chen, H. Xu, J. Suriyaprakash, H. Wu, L. Dong, X. Li, D. Li, Z. Wu, Rationalized carrier confinement significantly enhances overall photocatalytic water splitting in branched $\text{CdS}/\text{C}_3\text{N}_5$, *Sep. Purif. Technol.* 344 (2024) 127267.
- [15] J.H. Kim, J.S. Lee, Elaborately modified BiVO_4 photoanodes for solar water splitting, *Adv. Mater.* 31 (2019) 1806938.
- [16] Y. Qi, J. Zhang, Y. Kong, Y. Zhao, S. Chen, D. Li, W. Liu, Y. Chen, T. Xie, J. Cui, Unraveling of cocatalysts photodeposited selectively on facets of BiVO_4 to boost solar water splitting, *Nat. Commun.* 13 (2022) 484.
- [17] A. Hezam, K. Namratha, Q.A. Drmosh, B.N. Chandrashekhar, K.K. Sadasivuni, Z. H. Yamani, C. Cheng, K. Byrappa, Heterogeneous growth mechanism of ZnO nanostructures and the effects of their morphology on optical and photocatalytic properties, *CrystEngComm* 19 (2017) 3299–3312.
- [18] L.W. Shan, J.J. Bi, C.H. Lu, Y.W. Xiao, $\text{BiVO}_4(010)/\text{GO}$ nanocomposite and its photocatalytic application, *J. Inorg. Organomet. Polym.* 29 (2019) 1000–1009.
- [19] A. Kudo, K. Omori, H. Kato, A novel aqueous process for preparation of crystal form-controlled and highly crystalline BiVO_4 powder from layered vanadates at room temperature and its photocatalytic and photophysical properties, *J. Am. Chem. Soc.* 121 (1999) 11459–11467.
- [20] L. Shan, J. Li, Z. Wu, L. Dong, H. Chen, D. Li, J. Suriyaprakash, X. Zhang, Unveiling the intrinsic band alignment and robust water oxidation features of hierarchical BiVO_4 phase junction, *Chem. Eng. J.* 436 (2022) 131516.
- [21] L.W. Shan, C.H. Lu, L.M. Dong, J. Suriyaprakash, Efficient facet regulation of BiVO_4 and its photocatalytic motivation, *J. Alloy. Comp.* 804 (2019) 385–391.
- [22] S. Bai, H. Chu, X. Xiang, R. Luo, J. He, A. Chen, Fabricating of $\text{Fe}_2\text{O}_3/\text{BiVO}_4$ heterojunction based photoanode modified with NiFe-LDH nanosheets for efficient solar water splitting, *Chem. Eng. J.* 350 (2018) 148–156.
- [23] M. Yuan, J. Suriyaprakash, L. Shan, H. Xu, X. Li, H. Wu, G. Ding, Z. Shi, L. Dong, F. M. Zhang, Carrier confinement activated explicit solvent dynamic of $\text{CdS}/\text{BiVO}_4/\text{H}_2\text{O}$ and optimized photocatalytic hydrogen evolution performances, *J. Colloid Interf. Sci.* 658 (2024) 571–583.
- [24] A. Nagar, S. Basu, Ternary $\text{g-C}_3\text{N}_4/\text{Ag}/\text{BiVO}_4$ nanocomposite: fabrication and implementation to remove organic pollutants, *Environ. Technol. Inno.* 23 (2021) 101646.
- [25] M. Fang, Q. Cai, Q. Qin, W. Hong, W. Liu, Mo-doping induced crystal orientation reconstruction and oxygen vacancy on BiVO_4 homojunction for enhanced solar-driven water splitting, *Chem. Eng. J.* 421 (2021) 127796.
- [26] L.W. Shan, G.L. Wang, J. Suriyaprakash, D. Li, L.Z. Liu, L.M. Dong, Solar light driven pure water splitting of B-doped BiVO_4 synthesized via a sol–gel method, *J. Alloy. Comp.* 636 (2015) 131–137.
- [27] Q. Pan, K. Yang, G. Wang, D. Li, J. Sun, B. Yang, Z. Zou, W. Hu, K. Wen, H. Yang, BiVO_4 nanocrystals with controllable oxygen vacancies induced by Zn-doping coupled with graphene quantum dots for enhanced photoelectrochemical water splitting, *Chem. Eng. J.* 372 (2019) 399–407.
- [28] C. Zhou, Z. Sanders-Bellis, T.J. Smart, W. Zhang, L. Zhang, Y. Ping, M. Liu, Interstitial lithium doping in BiVO_4 thin film photoanode for enhanced solar water splitting activity, *Chem. Mater.* 32 (2020) 6401–6409.
- [29] A. Polo, I. Grigioni, M. Magni, A. Facibeni, M.V. Dozzi, E. Sellì, Unravelling the bulk and interfacial charge transfer effects of molybdenum doping in BiVO_4 photoanodes, *Appl. Surf. Sci.* 556 (2021) 149759.
- [30] X. Yin, W. Qiu, W. Li, C. Li, K. Wang, X. Yang, L. Du, Y. Liu, J. Li, High porosity Mo doped BiVO_4 film by vanadium re-substitution for efficient photoelectrochemical water splitting, *Chem. Eng. J.* 389 (2020) 124365.
- [31] C. Regmi, Y.K. Kshetri, T.-H. Kim, R.P. Pandey, S.W. Lee, Visible-light-induced Fe-doped BiVO_4 photocatalyst for contaminated water treatment, *Mol. Catal.* 432 (2017) 220–231.
- [32] Yan Xue, Xitao Wang, The effects of Ag doping on crystalline structure and photocatalytic properties of BiVO_4 , *Int. J. Hydrol. Energ.* (2015).
- [33] C. Zhang, Y. Shi, Y. Si, M. Liu, L. Guo, J. Zhao, O.V. Prezhdo, Improved carrier lifetime in BiVO_4 by spin protection, *Nano Lett.* 22 (2022) 6334–6341.
- [34] X. Zhang, G. Lu, The spin-orbit coupling induced spin flip and its role in the enhancement of the photocatalytic hydrogen evolution over iodinated graphene oxide, *Carbon* 108 (2016) 215–224.
- [35] W. Zhang, W. Gao, X. Zhang, Z. Li, G. Lu, Surface spintronics enhanced photocatalytic hydrogen evolution: mechanisms, strategies, challenges and future, *Appl. Surf. Sci.* 434 (2018) 643–668.
- [36] C.-C. Lin, T.-R. Liu, S.-R. Lin, K.M. Boopathi, C.-H. Chiang, W.-Y. Tzeng, W.-H. C. Chien, H.-S. Hsu, C.-W. Luo, H.-Y. Tsai, H.-A. Chen, P.-C. Kuo, J. Shieh, J.-W. Chiou, W.-F. Pong, C.-C. Chen, C.-W. Chen, Spin-polarized photocatalytic CO_2 reduction of Mn-doped perovskite nanoplates, *J. Am. Chem. Soc.* 144 (2022) 15718–15726.
- [37] R. Li, F. Zhang, D. Wang, J. Yang, M. Li, J. Zhu, X. Zhou, H. Han, C. Li, Spatial separation of photogenerated electrons and holes among (010) and (110) crystal facets of BiVO_4 , *Nat. Commun.* 4 (2013) 1432.
- [38] S. Nosé, A unified formulation of the constant temperature molecular dynamics methods, *J. Chem. Phys.* 81 (1984) 511–519.
- [39] W.G. Hoover, Canonical dynamics: equilibrium phase-space distributions, *Phys. Rev. A* 31 (1985) 1695–1697.
- [40] M.G. Lee, C.W. Moon, H. Park, W. Sohn, S.B. Kang, S. Lee, K.J. Choi, H.W. Jang, Dominance of plasmonic resonant energy transfer over direct electron transfer in substantially enhanced water oxidation activity of BiVO_4 by shape-controlled au nanoparticles, *Small* 13 (2017) 1701644.
- [41] G. Zhang, Y. Meng, B. Xie, Z. Ni, H. Lu, S. Xia, Precise location and regulation of active sites for highly efficient photocatalytic synthesis of ammonia by facet-dependent BiVO_4 single crystals, *Appl. Catal. B: Environ.* 296 (2021) 120379.
- [42] M. Barawi, M. Gomez-Mendoza, F.E. Oropeza, G. Gorni, I.J. Villar-Garcia, S. Gimenez, V.A. de la Pena O'Shea, M. Garcia-Tecedor, Laser-Reduced BiVO_4 for enhanced photoelectrochemical water splitting, *ACS Appl. Mater. Interfaces* 14 (29) (2022) 33200–33210.
- [43] M. Noor, F. Sharmin, M.A.A. Mamun, S. Hasan, M.A. Hakim, M.A. Basith, Effect of Gd and Y Co-doping in BiVO_4 photocatalyst for enhanced degradation of methylene blue dye, *J. Alloy. Comp.* 895 (2022) 162639.
- [44] X. Ouyang, C. Feng, X. Zhu, Y. Liao, Z. Zhou, X. Fan, Z. Zhang, L. Chen, L. Tang, 3D printed bionic self-powered sensing device based on fern-shaped nitrogen doped BiVO_4 photoanode with enriched oxygen vacancies, *Biosens. Bioelectron.* 220 (2022) 114817.
- [45] N. Ma, J. Xu, Z. Bian, Y. Yang, L. Zhang, H. Wang, BiVO_4 plate with Fe and Ni oxyhydroxide cocatalysts for the photodegradation of sulfadimethoxine antibiotics under visible-light irradiation, *Chem. Eng. J.* 389 (2020) 123426.
- [46] L. Gao, X. Long, S. Wei, C. Wang, T. Wang, F. Li, Y. Hu, J. Ma, J. Jin, Facile growth of AgVO_3 nanoparticles on Mo-doped BiVO_4 film for enhanced photoelectrochemical water oxidation, *Chem. Eng. J.* 378 (2019) 122193.
- [47] L. Zhang, W. Wang, D. Jiang, E. Gao, S. Sun, Photoreduction of CO_2 on BiOCl nanoplates with the assistance of photoinduced oxygen vacancies, *Nano Res.* 8 (2015) 821–831.
- [48] A. Kahraman, M.B. Vishlaghi, I. Baylam, H. Ogasawara, A. Sennaroğlu, S. Kaya, The fast-track water oxidation channel on BiVO_4 opened by nitrogen treatment, *J. Phys. Chem. Lett.* 11 (2020) 8758–8764.
- [49] Y. Sun, H. Li, Y. Hu, J. Wang, A. Li, P.F.-X. Corvini, Single-atomic ruthenium coupling with NiFe layered double hydroxide in-situ growth on BiVO_4 photoanode for boosting photoelectrochemical water splitting, *Appl. Catal. B: Environ.* 340 (2024) 123269.
- [50] C. Lai, M. Zhang, B. Li, D. Huang, G. Zeng, L. Qin, X. Liu, H. Yi, M. Cheng, L. Li, Fabrication of CuS/BiVO_4 (040) binary heterojunction photocatalysts with enhanced photocatalytic activity for Ciprofloxacin degradation and mechanism insight, *Chem. Eng. J.* 358 (2019) 891–902.
- [51] Y. Yang, Z. Zheng, M. Yang, J. Chen, C. Li, C. Zhang, X. Zhang, In-situ fabrication of a spherical-shaped Zn-Al hydroxalcite with BiOCl and study on its enhanced photocatalytic mechanism for perfluorooctanoic acid removal performed with a response surface methodology, *J. Hazard. Mater.* 399 (2020) 123070.

[52] Z. Jiang, B. Cheng, Y. Zhang, S. Wageh, A.A. Al-Ghamdi, J. Yu, L. Wang, S-scheme ZnO/WO₃ heterojunction photocatalyst for efficient H₂O₂ production, *J. Mater. Sci. Technol.* 124 (2022) 193–201.

[53] Y. Jia, Z. Wang, X. Qiao, L. Huang, S. Gan, D. Hou, J. Zhao, C. Sun, D. Li, A synergistic effect between S-scheme heterojunction and Noble-metal free cocatalyst to promote the hydrogen evolution of ZnO/CdS/MoS₂ photocatalyst, *Chem. Eng. J.* 424 (2021) 130368.

[54] Q. Li, X.-Q. Qiao, Y. Jia, D. Hou, D.-S. Li, Amorphous CoMoS₄ nanostructure for photocatalytic H₂ generation, nitrophenol reduction, and methylene blue adsorption, *ACS Appl. Nano Mater.* 3 (2020) 68–76.

[55] S. Yuan, J. Zou, N. Lin, H. Zhang, D. Li, Y. Wu, Understanding the protective role of a gradient titanium oxide ceramic layer on Ti₆Al₄V against corrosion via analyses of Mott-Schottky curve and electron work function (EWF), *Ceram. Int.* 48 (2022) 31896–31901.

[56] P. Zhu, D. Luo, M. Liu, M. Duan, J. Lin, X. Wu, Flower-globular BiOI/BiVO₄/g-C₃N₄ with a dual Z-scheme heterojunction for highly efficient degradation of antibiotics under visible light, *Sep. Purif. Technol.* 297 (2022) 121503.

[57] Z. Liang, Y. Xue, X. Wang, X. Zhang, J. Tian, Structure engineering of 1T/2H multiphase MoS₂ via oxygen incorporation over 2D layered porous g-C₃N₄ for remarkably enhanced photocatalytic hydrogen evolution, *Mater. Today Nano* 18 (2022) 100204.

[58] Y. Zhou, P. Yan, J. Jia, S. Zhang, X. Zheng, L. Zhang, B. Zhang, J. Chen, W. Hao, G. Chen, Q. Xu, B. Han, Supercritical CO₂-constructed intralayer [Bi₂O₂]²⁺ structural distortion for enhanced CO₂ electroreduction, *J. Mater. Chem. A* 8 (2020) 13320–13327.

[59] L.W. Shan, Y.T. Liu, J.J. Bi, J. Suriyaprakash, Z.D. Han, Enhanced photocatalytic activity with a heterojunction between BiVO₄ and BiOI, *J. Alloy. Comp.* 721 (2017) 784–794.

[60] J. Zhang, L. Shan, H. Xu, X. Li, Z. Fang, H. Wu, D. Li, L. Dong, C. Cheng, J. Suriyaprakash, F.M. Zhang, Multiscale understand the tuning photocatalytic hydrogen evolution performances of BiOCl stemmed from engineered crystal facet, *Appl. Surf. Sci.* 652 (2024) 159321.

[61] H. Su, W. Che, F. Tang, W. Cheng, X. Zhao, H. Zhang, Q. Liu, Valence band engineering via Pt^{II} single-atom confinement realizing photocatalytic water splitting, *J. Phys. Chem. C* 122 (2018) 21108–21114.

[62] K. Sekar, A. Kassam, Y. Bai, B. Coulson, W. Li, R.E. Douthwaite, K. Sasaki, A.F. Lee, Hierarchical bismuth vanadate/reduced graphene oxide composite photocatalyst for hydrogen evolution and bisphenol A degradation, *Appl. Mater. Today* 22 (2021) 100963.

[63] X. Wu, J. Zhao, S. Guo, L. Wang, W. Shi, H. Huang, Y. Liu, Z. Kang, Carbon dot and BiVO₄ quantum dot composites for overall water splitting via a two-electron pathway, *Nanoscale* 8 (2016) 17314–17321.

[64] H. Hou, L. Wang, F. Gao, X. Yang, W. Yang, BiVO₄@TiO₂ core–shell hybrid mesoporous nanofibers towards efficient visible-light-driven photocatalytic hydrogen production, *J. Mater. Chem. C* 7 (2019) 7858–7864.

[65] S. Chen, D. Huang, P. Xu, X. Gong, W. Xue, L. Lei, R. Deng, J. Li, Z. Li, Facet-engineered surface and interface design of monoclinic scheelite bismuth vanadate for enhanced photocatalytic performance, *ACS Catal.* 10 (2020) 1024–1059.

[66] Y. Yuan, Y. Huang, F. Ma, Z. Zhang, X. Wei, Effects of oxygen vacancy on the mechanical, electronic and optical properties of monoclinic BiVO₄, *J. Mater. Sci.* 52 (2017) 8546–8555.

[67] R. Hill, The elastic behaviour of a crystalline aggregate, *Proc. Phys. Soc. Sect. A* 65 (1952) 349.

[68] S.F. Pugh, XCII. Relations between the elastic moduli and the plastic properties of polycrystalline pure metals, *Philos. Mag.* 45 (1954) 823–843.

[69] A. Marmier, Z.A.D. Lethbridge, R.I. Walton, C.W. Smith, S.C. Parker, K.E. Evans, ELAM: A computer program for the analysis and representation of anisotropic elastic properties, *Comput. Phys. Commun.* 181 (2010) 2102–2115.

[70] X. Song, X. Fu, M. Wang, First-principles study of β' phase in Mg–RE alloys, *Int. J. Mech. Sci.* 243 (2023) 108045.